PROCEEDINGS OF SPIE

SPIEDigitalLibrary.org/conference-proceedings-of-spie

Simulation of infrared avalanche photodiodes from first principles

Asta Katrine Storebø
Dara Goldar
Trond Brudevoll

SPIE.

Simulation of infrared avalanche photodiodes from first principles

Asta Katrine Storebø*[a], Dara Goldar[b], and Trond Brudevoll[a],
[a]FFI (Norwegian Defence Research Establishment), P.O. Box 25, N-2027 Kjeller, Norway; [b]NTNU (Norwegian University of Science and Technology), Høgskoleringen 1, 7034 Trondheim, Norway

ABSTRACT

The present article deals with device physics and modeling of an $Hg_{0.28}Cd_{0.72}Te$ wide-area electron-initiated avalanche photodiode, with main input data extracted from first principles electronic structure codes. Due to the large dimensions of 30 µm x 30 µm x 11 µm a method which combines Monte Carlo transport simulation in the active multiplication layer with 'weak conduction' modeling in the charge carrier exit paths is introduced. Consequences resulting from adding perturbative, non-self-consistent small-signal analyses upon a self-consistent, large-signal background bias simulation are briefly examined. Likewise, the issue of ambipolar versus independent electron-hole transport in the absorption layer is discussed. We investigate the effects of alloy scattering on avalanche gain and compare alloy scattering rates used in some recent studies. Alloy scattering is for this particular device and model shown to increase the gain by more than an order of magnitude at typical bias voltages.

Keywords: HgCdTe, avalanche photodiode, APD, infrared detector, first principles

1. INTRODUCTION

We study a planar, back-illuminated n-on-p $Hg_{0.28}Cd_{0.72}Te$ avalanche photodiode using material properties data derived directly from first principles electronic structure calculations. By such calculations the use of experimentally measured parameters can largely be avoided, and more detail can be fed into the simulation. Full-band Monte Carlo (MC) device simulation can readily proceed from this kind of detailed information in contrast to other methods which would need an additional intermediate step where materials data are first lumped onto average ensemble-based steady-state/near-equilibrium properties.

Our full-band MC particle simulator is intended for use within the fields of materials technology and semiconductor optoelectronic devices. The simulator takes input data from first principles pseudopotential (ABINIT[1]) or linearized plane wave (Wien2k[2]) packages. Electric fields are calculated either via finite difference or finite element methods which are fully integrated into the code.

Due to the extremely long penetration depth of infrared (IR) photons, the thickness of the diode absorption layers is typically quite large. This represents a considerable computational challenge if detailed MC simulation models are to be used over the whole volume of the device. Different ways of dealing with this problem are considered. The optical signal creates an electronic disturbance which is tracked as it propagates through the p-doped absorption layer of the device. Strongly non-equilibrium regions, near equilibrium regions, ambipolar transport, impact ionization, dynamic field effects and alloy scattering must all be given proper attention, and the importance of each of these elements are discussed.

2. TWO APPROACHES FOR SOLVING THE BOLTZMANN EQUATION

The electronic transport properties of semiconductors are determined by the solution of the Boltzmann transport equation (BTE) for the system. The BTE is commonly solved using two very different approaches, either by explicitly solving the resulting momentum equations, or by performing MC simulations, see Figure 1. The MC method uses pseudorandom numbers to simulate the scattering of individual charge carriers and thereby indirectly solves the transport equation. MC simulation offers a great level of details, but tends to be very CPU intensive, memory intensive, and time consuming.

*asta-katrine.storebo@ffi.no; phone 47 63 80 72 94; fax 47 63 80 72 12; ffi.no

Infrared Technology and Applications XLIII, edited by Bjørn F. Andresen, Gabor F. Fulop, Charles M. Hanson, John L. Miller, Paul R. Norton, Proc. of SPIE Vol. 10177, 101771B · © 2017 SPIE
CCC code: 0277-786X/17/$18 · doi: 10.1117/12.2262473

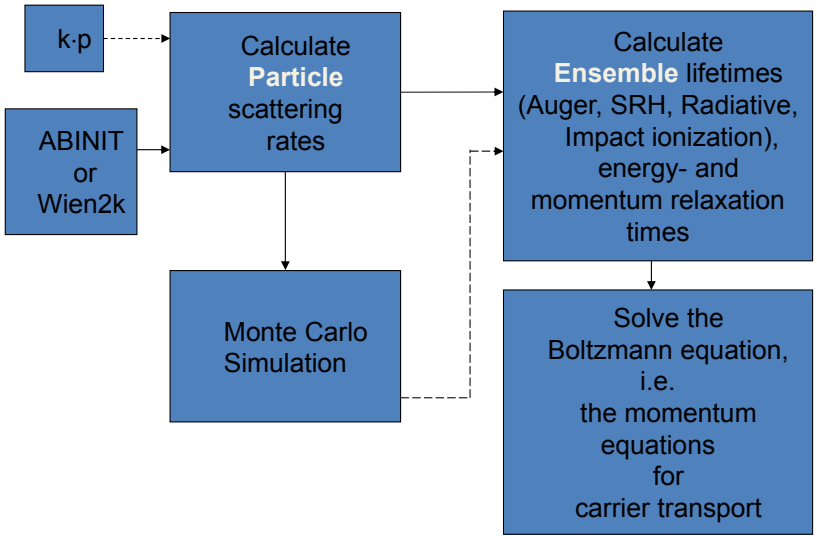

Figure 1. Stages from first principles electronic structure calculation, via input data extraction to device simulation either using MC simulation or by solving the momentum equations.

3. FIRST PRINCIPLES BAND STRUCTURE MODELS AND MC SIMULATION

An important merit of full-band MC simulators is the ability to take input data directly from first-principles electronic structure codes. Thus we obtain an exact representation of the bands over the whole Brillouin zone, valid for any crystalline or alloy material. This representation also provides the opportunity to study both spin channels in a given band, a feature relevant for future spin-based electronics or in laser-matter interactions when the incoming radiation is circularly or elliptically polarized. Circularly polarized radiation is of interest in areas such as quantum optical computing, optical spintronics, biomedicine, and high efficiency displays.

ABINIT is one of the electronic structure packages providing input data for the MC simulator. ABINIT is a pseudopotential code, and it has produced the band structures for all the simulations presented here. In addition, we have devoted much work to adapt another first principles code, Wien2k, which is based on a linearized augmented plane wave (LAPW) method. Not only band energies, but also various scattering matrix elements representing the carrier interactions must be extracted before the MC simulation can begin. Whereas optical matrix elements are usually readily available from the first-principles packages, numeric calculation of the many electronic interaction matrix elements is a much harder problem.

With respect to a crystalline material like HgTe or CdTe, both having the ordered ZnS structure, the alloy $Hg_{1-x}Cd_xTe$ (MCT) is a disordered material. Fundamental properties, like the band gap, change when Cd is introduced into HgTe. What we need then, is an appropriately taken average representing the overall band structure, and upon that a representation of the alloy disorder. The electronic response to alloy disorder manifests itself as a separate process; alloy scattering. Pseudopotentials can be averaged to give an overall band structure as if the alloy were a virtual ZnS crystal, but for an all-electron code like Wien2k, one must deal with fractional electrons and the versatility of the method would be very limited in that case. Instead, calculating many different geometrical configurations of Hg and Te in larger supercells of MCT, and folding the various supercell band structures back into the larger Brillouin zone of the ZnS structure is an option which has become available lately[3]. A proper average can then be taken within the backfolded configurations of the ZnS cell.

Most first principles band structure calculations are based upon density functional theory (DFT), an approach which is known to underestimate the band gap in semiconductors. In addition, DFT has a shortcoming in the description of the correlation within deep-lying, localized electrons in *d*-states, 5*d* in Hg and 4*d* in Cd. The lack of felt repulsion between such DFT electrons results in these *d*-states lying much too high in energy. This can be corrected by introducing the Hubbard U, i.e. a DFT+U approach. We noted that with Wien2k, applying the U-correction to pull the *d*-levels down increased the fundamental band gap somewhat, apparently through the corrected levels' effect on the total potential.

Turning now our attention to the underestimation of the band gap, using a modified Becke-Johnson potential[4] (mBJ) should correct this deficiency. The total approach would then be backfolding+DFT+U+mBJ to obtain the correct band gap at T=0. We note that this method would be cheap enough to be combined with supercell calculations, which is not the case for more sophisticated, expensive methods like *GW* (Green's function and screened interaction *W*) or Bethe-Salpeter equation.

Temperature corrections of band gaps and effective masses have been much less eagerly pursued. Some trends in band gaps can be predicted economically though, but again expensive methods are available too in some codes. In any case, one should avoid doing a simple rigid scissors operator shift if the gap correction is large. The effective mass will increase with increasing band gap, as is seen experimentally and also predicted by Kane's perturbation theory. Over-exaggerating the T=0 corrections (U+mBJ) could provide a temporary relief, with a plausible effective mass, see Figure 2, which gives an example of a corrected band structure for $Hg_{0.72}Cd_{0.28}Te$ at 77 K temperature using Wien2k. Obviously, some work should be done here to see if similar economic methods could do the trick in a less *ad-hoc* way.

The current MC simulator is based on a semiclassical transport approach. It has been initially tested on bulk HgCdTe material, on HgCdTe n-on-p avalanche photodiodes, and on HgCdTe Thz switches. MC simulation has traditionally been a tool for studying small electronic devices. Here we need to describe the other end of the length scale, the larger dimensions typically encountered in optoelectronic devices. MC models are suited for giving a detailed representation of all interactions, but are limited with respect to the size of the devices that they can handle. The size limitations are closely linked to the available RAM memory and execution speed of the computers at hand, but this also means that these limitations are expected to be gradually relaxed over time. Cases that can be simulated range from CMOS transistors at 10 nm gate length to large photodetector elements at dimensions up to a few µm. This means that most electronic and optoelectronic devices can be analyzed, provided special care is taken with the largest photodetector elements beyond 10 µm, and especially at low signal levels. Bulk materials can be treated without regard to size.

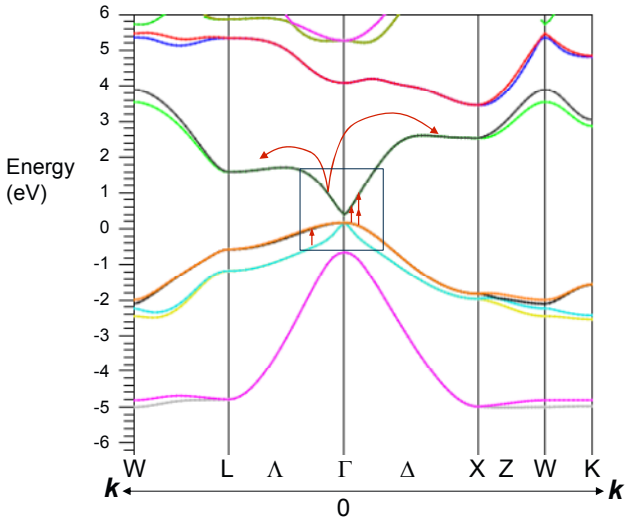

Figure 2. Band structure from Wien2k for $Hg_{0.72}Cd_{0.28}Te$ at 77 K.

For the photodetector elements at normal signal levels it is necessary to divide the analysis into two stages; a large signal steady-state bias simulation followed by a small-signal simulation. Usually, bias simulations are carried out solving the momentum equations, combined with an MC simulation of the signals, but here we shall use MC simulation on both.

4. MCT APD DESIGN

The design under study is depicted in Figure 3. It has a Cd alloy fraction x=0.28, a 30 µm x 30 µm surface area, and a 6.2 µm thick p-type doped absorption layer. The free carrier concentration in the absorption layer is $p=2.0\cdot10^{16}$ cm^{-3}. In the 4 µm thick, lightly n-doped multiplication layer the free carrier concentration is $n=5\cdot10^{14}$ cm^{-3}.

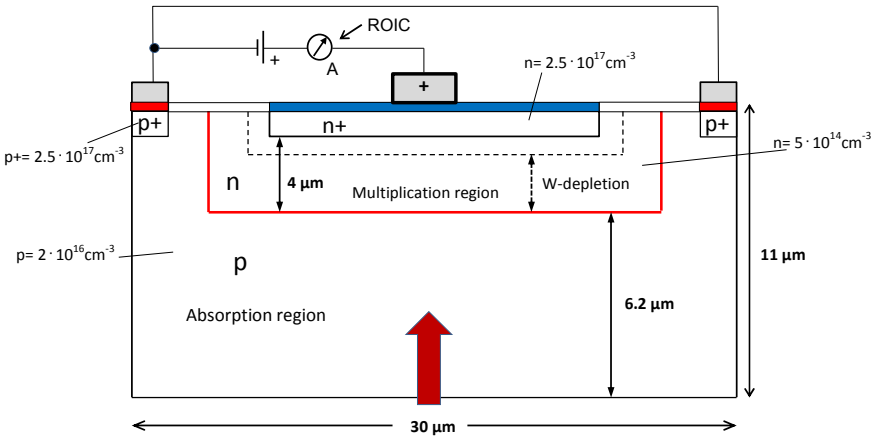

Figure 3. Planar electron-initiated APD with bias voltage supply and read-out IC (ROIC). Radiation enters the device through the lower surface (red arrow).

The width of the n-doped region reduces to 2.5 µm in the vertical corridor near the two p^+ side contacts. This is done in order to keep the n^+- section as wide as possible, thereby ensuring a more uniform spatial response. Near the contacts we include sections with higher doping, corresponding to free carrier densities n^+ and p^+ of $2.5 \cdot 10^{17}$ cm^{-3}.

The primary, photogenerated electrons created in the absorption layer must pass through the multiplication region in order to be collected at the center contact. Holes are collected by either of the two p^+ side contacts. Primary, photogenerated holes do not enter the multiplication region at all. Secondary, off-spring holes generated by electron-initiated impact ionization inside the multiplication region must first travel downwards through that region and into the absorption region. Then they follow a long, resistive path into this region and towards the two side contacts. If they fail to be collected at the side contacts, there will be a signal loss, as each generated electron-hole pair must complete a full path from their point of generation towards their respective collecting electrodes in order to push one electron through the readout electronics.

5. THEORY AND NUMERICAL MODEL

We have used a MC carrier transport simulator for both the large-signal (bias) and small signal analysis of the APD. The bias calculation was carried out in the superparticle picture where each superparticle represents a large number of charge carriers. Band structures for the MCT alloy were imported directly from the *ab initio* pseudopotential electronic structure code ABINIT, after introducing band-gap corrections appropriate for the particular alloy composition and temperature. Impact ionization is described with the Keldysh relation[5,6].

5.1. Ambipolar transport of initial photogenerated charge carriers in absorption layer

We have assumed that charge carriers move as independent particles. This condition is normally fulfilled when the semiconductor is strongly and/or uniformly irradiated. If the radiation is weak the photoinduced carrier density can become smaller than the background p-type doping density, and then the transport will show ambipolar behavior[7]. The same thing happens if the radiation is localized on some part of the semiconductor. The avalanche response of an e-APD starts when the initial photogenerated electron reaches the multiplication layer. Being a small disturbance in the p-type background of holes, transport of a photogenerated electron under weak and/or localized radiation is governed by ambipolar drift and diffusion laws. Here the excess photogenerated electron will still move as under independent transport, just as it did in the limit of very high/uniform irradiation levels. Excess holes however, will be located around the photogenerated electrons as a screening charge when the transport mode turns ambipolar.

As the potential in much of the absorption layer is rather flat, minor timing differences regarding the onset of the APD avalanche may well be present due to ambipolar diffusion, but by and large we expect that electrons will have the same mobility and diffusion constant in the p-type absorption layer as they would have for independent transport.

In our approximation, electron-hole scattering within the electron-hole packet has been neglected. It has been known for some time now that such simplifications may sometimes lead to wrong predictions for the direction of movement of the electron-hole disturbance in quantum wells[8,9].

5.2. Background carriers respond to movement of avalanche generated carriers

In order to take background carrier effects of wide-area (3D) devices into account, we have modeled the arrival of avalanche generated charge carriers onto the resistive areas surrounding the pn junction as charge injection into a weakly conducting medium[10,11] containing background carriers. Avalanche generated carriers in the multiplication region are assumed to follow a pre-determined movement pattern as prescribed by the MC simulation, and the background carries must respond accordingly. This produces an equivalent circuit diagram as in Figure 4.

Alternatively, one could have ignored the background charge carriers in the small-signal analysis and treated the resistive exit paths as good conductors by considering the hole collecting side electrodes to be placed directly at the pn junction, but then one would totally have missed the capacitive effects of the exit paths. In our approach the current is smoothed out and distributed among all carriers present, both background carriers and injected carriers. Voltages over the resistive areas and the displacement currents due to the internal capacitances shown in Figure 4 are calculated directly, differing slightly from the method outlined in[10].

As the total voltage over the device is considered constant, the current-driving voltages shifting over to the resistive exit paths during the optical impulse will lead to a locally reduced or 'screened' bias electric field over the pn junction, thereby causing gain saturation. This represents a negative feedback on the gain, and such nonlinearities can be induced either by high gain or high photon fluxes, as seen in simulations of smaller GaN avalanche APDs[12]. In wide-area devices these effects can easily get lost due to finite computer resources allowing only stationary, non-self-consistent bias electric fields to be calculated. If gain saturation effects are to be included, the basically linear, non-self-consistent procedure used here would have to be corrected to obtain the reduced injection current. The need for corrections will show up as non-negligible voltage drops over the exit paths.

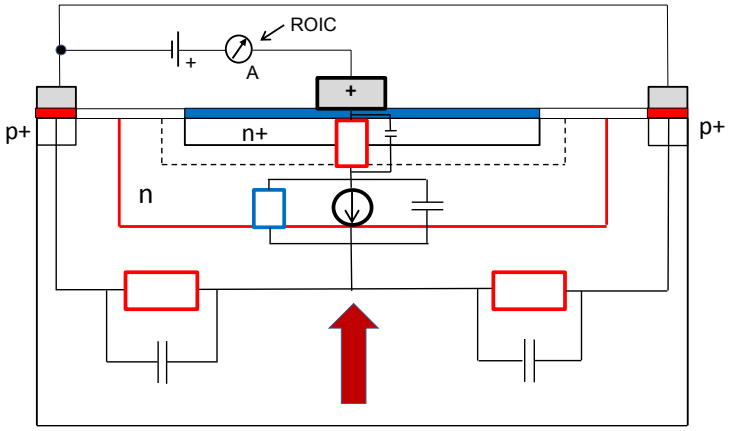

Figure 4. Equivalent circuit diagram of reverse biased APD with exit path series resistances shown in red and shunt resistance shown in blue, with accompanying capacitances. The output of the indicated current source is governed by the applied bias and the incident radiation. Hole collecting electrode; red, electron collecting electrode; blue.

Finally we note that the displacement current $\frac{\partial \boldsymbol{D}}{\partial t}$ after an IR pulse will not affect the total, integrated charge transfer through the external wires, because the electric displacement $\boldsymbol{D}$ must return to its initial value after the pulse. It will however cause the external current signal to become slightly shifted forward in time.

5.3. Importance of elastic scattering mechanisms

Other influences affecting gain in quite a different manner from the gain saturation described above are the two classes of elastic scattering occurring either via impurities or via alloy fluctuations. Elastic scattering does not change the kinetic energy of a charge carrier within a single given scattering event, but if we consider the aftermath of a full 180 degree backward scattering in **k**-space it becomes apparent that a charge carrier with initial momentum **k** must go through a cycle of reduced kinetic energy as it passes from the scattered state –**k** back to **k** in the electric field. During this cycle, its probability of generating impact ionization is strongly reduced. In other words: Turning on alloy scattering reduces

the electrical mobility, which cools down the electronic distribution function and temporarily reduces impact ionization. The impact ionization coefficient indicates the probability of impact ionization per unit length travelled by a charge carrier at a given electric field. Depending somewhat on the details of how it is defined[6], the coefficient can become drastically reduced when alloy scattering is turned on, as was pointed out in the GaAlN MC bulk simulations of Bulutay[13] and also neatly demonstrated recently for the same bulk material by 'dead-space' corrected impact ionization coefficients extracted from MC simulations[14]. In the present work we do not need the concept of impact ionization coefficients at all, since we have used a 'microscopic' MC approach directly in the device simulation instead. Therefore we stick to a scattering *rate* for describing impact ionization. What comes into play in our description is how the changed carrier distribution function influences gain by altering individual electron paths and increasing the time the electron spends in the APD multiplication region.

If the angular dependence of the scattering mechanism is uniform as in the alloy scattering model used here, we would expect a much stronger influence on the gain than for a mechanism such as ionized impurity scattering, which favors only forward scattering and in addition decreases rapidly at high carrier energies. We have used alloy scattering potentials derived from[15,16], with a valence band offset of 0.35 eV, giving carrier mobilities in accord with accepted experimental data. Alloy scattering was reviewed and discussed in[17], and a model showing angular dependence at high energies was demonstrated in[18]. In later years an analysis based on the electronic structure was carried out for AlGaAs alloys by Bellotti et al.[19].

6. RESULTS

From the preceding sections it follows that the transport of primary photogenerated carriers in the absorption layer will depend somewhat on irradiation duration and irradiation level. We assume only one impinging photon in the following, thus testing the impulse response of the device and not the response to irradiation with finite pulse duration.

6.1 Internal charge carrier distribution

In Figure 5 we have plotted particle positions of the off-spring free electrons and holes in the pn junction for 7 V reverse bias at 77 K. It is clearly seen that the distribution of carriers after 10-80 ps is not at all uniform along the z-axis.

From the angle of view chosen in Figure 5 a curious artifact regarding off-spring carrier generation can be observed: There are two distinct bursts of carrier generation; the first is related to the initial photoelectron entering the pn junction.

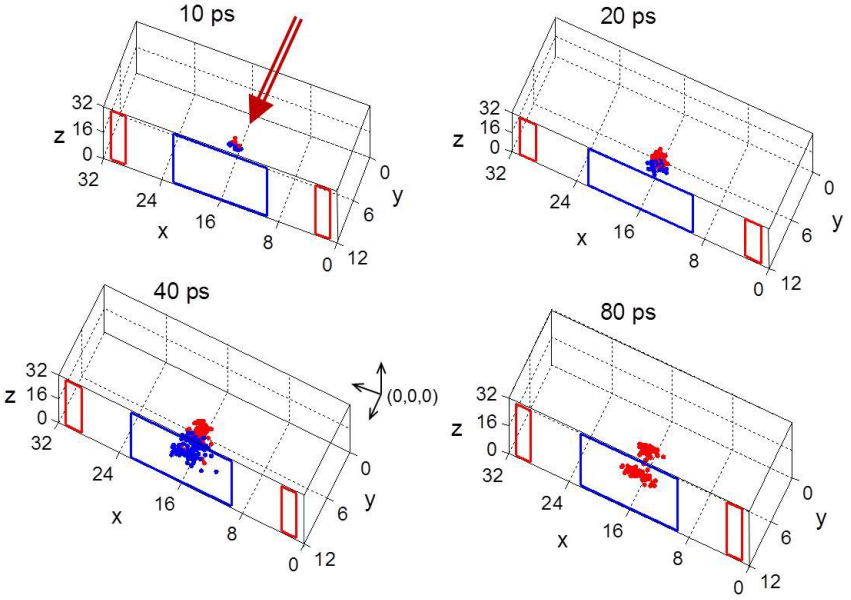

Figure 5. 3D particle positions of electrons and holes in the pn junction from 10-80 ps after initial photon absorption at (x,y,z) = (16, 6.7, 16) µm. The arrow indicates the direction of the incident radiation. Blue dots = electrons, red dots = holes. Hole collecting electrodes are drawn in red, and the electron-collecting mid-electrode is indicated in blue. Reverse bias was 7 V.

The second burst occurs when the generated carriers have been accelerated again in the strong junction electric field, but at some of the places where the last carriers are generated the field is actually very weak, as indicated by the slow retreat of the last generated holes back onto the p-type region observed at 80 ps.

These artifacts partly derive from the non-local field dependence of impact ionization, but also from the details of the layout near the end of the multiplication region. A local electric field due to the abrupt change from n^+ - doping to light n-doping in a narrow neutral semiconductor section outside the n^+ contact area can promote 'last minute' carrier generation in a similar way. From this simulation we can conclude that the relation between gain and geometry can be rather delicate, even if the layout seems simple and uniform at first glance.

Figure 6 gives a gain versus bias curve derived from our MC simulator. Each APD simulation consisted of 100 different single-photon absorption events at the same position.

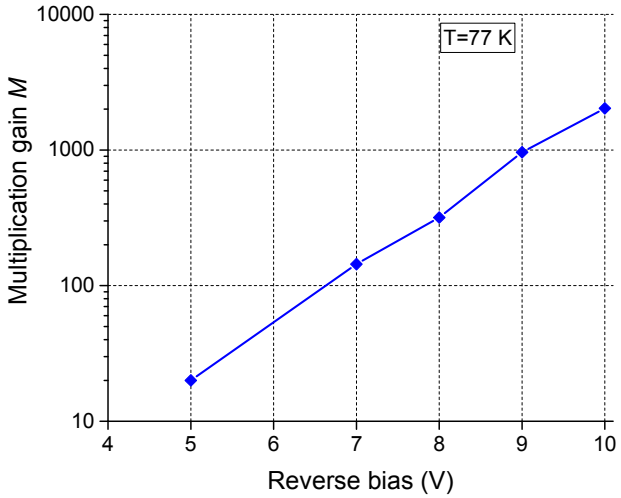

Figure 6. Simulated gain as a function of reverse bias in $Hg_{0.72}Cd_{0.28}Te$ at T=77 K.

6.2 Terminal currents

In order to illustrate the different responses of electrons and holes we present the arrival times of these carriers in a "bar code" plot, Figure 7, as they arrive onto the resistive areas on both sides of the pn junction. Red bars indicate holes and blue bars indicate electrons. Also shown is a smoothed envelope displaying the actual estimated current in the leads, with the strength of alloy gradients as in a previous publication[20]. Or rather, the current shown is in fact the sum of the currents in the negative "hole-collecting" electrodes as these are joined together, and the equally large current in the positive, "electron-collecting" mid-electrode".

As we can see, the movement of holes through the pn junction is more spread out in time, resulting in some signal loss at the main current peak. We do not see any indication of a speedup in hole response due to the alloy gradient field for holes. The strength of the hole and electron alloy gradient fields is determined by the band-lineup rules between two dissimilar materials and here all the speedup goes in favor of the electrons[15]. In addition, some of the exit paths followed by the secondary holes lies outside the region of high alloy gradients.

The plot of the external electrode current in Figure 6 gives the upper limit on how fast the APD can react to a radiation impulse of one photon, valid under the assumption that the contacts are held at constant voltages. However, this requires a large bandwidth, and it is to be expected that the external circuit would be the limiting factor in that respect[21]. With more incoming photons being absorbed at different locations in the absorption layer, the bursts generated by initial photoexcited carriers reaching the multiplication layer at different times will broaden the current peak to somewhat larger widths.

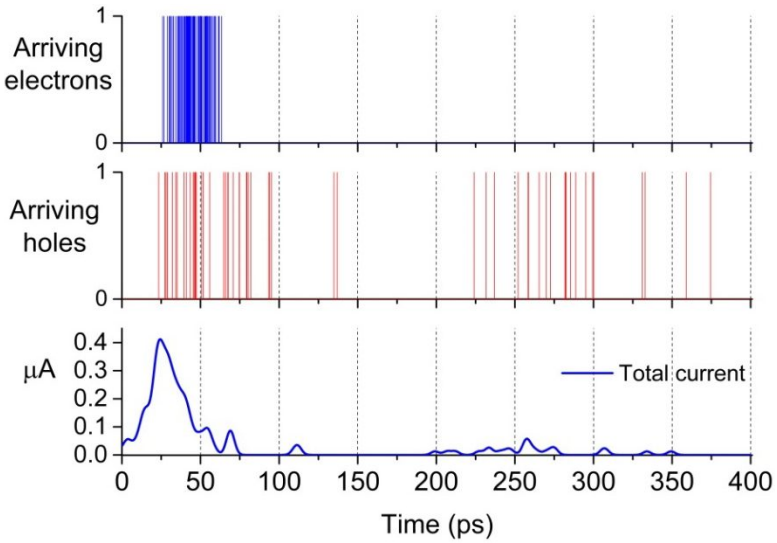

Figure 7. Above: Arrival of internal one-photon signal electrons (blue) and holes (red) from the pn junction onto the immediate surrounding resistive exit path areas leading towards the respective collecting electrodes. This particular signal had a gain $M = 111$. Initial electron-hole pair was generated at $x = 15$ μm, $y = 6.2$ μm. Below: Estimated terminal current due to this signal.

6.3 Effect of alloy scattering on gain

Table 1 shows results for the gain with and without alloy scattering, averaged over sets of 100 separate simulations. As we can see, the influence of this scattering mechanism is substantial, increasing the gain by a factor 16 at a reverse bias voltage of 7 V. There have not been many device simulations comparing results including alloy scattering with results excluding alloy scattering, but an increase in the gain by a factor of 5 at the same value of the reverse bias was obtained in[6] for a much smaller device than the one studied here. An analytic, isotropic description of the bands was used for those studies, with an alloy fraction $x = 0.3$. A slightly higher alloy fraction will naturally lead to somewhat higher electron alloy scattering rates, but the band gap also increases. The influence of alloy scattering on gain will depend quite sensitively on the actual electric field distribution of the device, and it will increase sharply with the applied bias[6].

Table 1. Gain with and without alloy scattering.

	Alloy	**No alloy**
M_{mean}	98	6
σ_{mean}	44	4
$F(M_{mean}) = 1+(\sigma_{mean}/ M_{mean})^2$	1.20	1.44

It is of interest to observe how the alloy scattering rate compares for two other band models used recently[6,22]. Table 2 shows the electron alloy scattering rates at four electron energies referenced to the conduction band edge. The band gap is 0.22 eV for x=0.28 and 0.24 eV for x=0.3.

Table 2. Electron alloy scattering rates from different references.

Energy	**0.1 eV**	**0.25 eV**	**0.5 eV**	**1eV**
Derelle et al. [10]	$2.5{\cdot}10^{12}$ s^{-1} (x=0.3)	$9.5{\cdot}10^{12}$ s^{-1}	$2.5{\cdot}10^{13}$ s^{-1}	$8.0{\cdot}10^{13}$ s^{-1}
Bertazzi et al. [2]	$2.5{\cdot}10^{12}$ s^{-1} (x=0.3)	$6.0{\cdot}10^{12}$ s^{-1}	$1.0{\cdot}10^{13}$ s^{-1}	$5.0{\cdot}10^{13}$ s^{-1}
This work	$1.0{\cdot}10^{12}$ s^{-1} (x=0.28)	$3.5{\cdot}10^{12}$ s^{-1}	$1.0{\cdot}10^{13}$ s^{-1}	$8.0{\cdot}10^{13}$ s^{-1}

At low electric fields, alloy scattering is just one of the mechanisms being important for reproducing the experimental mobilities. At higher energies, the relative importance of different scattering rates changes. In order to obtain a good agreement between theory and experiment for gain vs bias plots in materials without alloy scattering, a good model for impact ionization is of course crucial. But for materials with alloy scattering, we see here that it is not enough just to

have a good model for impact ionization. The simulation results will still only be as good as the alloy scattering model will allow, and the gain should also be sensitive to bias screening effects.

Although the alloy rates differ somewhat depending on the model used for the works we compare here, any angular dependence, say, will determine the efficiency of alloy scattering in increasing the gain. Even if alloy scattering influences the gain-voltage curves strongly, it is not expected to have much influence on the maximum achievable gain. The latter, usually occurring near the breakdown voltage, will just occur for a smaller bias voltage when alloy scattering is present, since alloy scattering will mainly shift the breakdown voltage to lower values.

7. CONCLUSIONS

Methods for particle based MC simulation of wide-area APDs at low signal levels were discussed, and we implemented a modified approach for signal current calculations.

APDs involve regions of very high electric fields, impact ionization, background carriers, regions of very low fields, as well as simultaneous transport of electrons and holes, all of which can in principle be well represented within an MC model. Any hybridization with other methods however, made necessary due to limited computer power, will inevitably result in a more coarse description resulting in some loss of detail.

It was shown that alloy scattering using a standard scattering model gave a significant increase in avalanche gain. It would seem likely that the gain should depend strongly on the particular impact ionization model used (here the Keldysh model), but the present results further suggest that a precise model of alloy scattering will be important.

From the discussion it also follows that the gain will be self-sensitive to the amount of avalanche carriers produced, a kind of negative feedback effect occurring via nonlinear changes in the voltage lying over the pn junction. With the method for terminal current calculations used here, this effect can be monitored and kept under control.

Although most of the features of wide-area APDs can be modeled precisely, obtaining a good overall agreement in avalanche gain vs. bias voltage curves up to high voltages without parameter fitting needs an accurate model of 1) impact ionization, 2) alloy scattering, and 3) the time varying feed-back effects on the electric field.

Let us also bear in mind that the ideal, fast one-photon response of the device demonstrated here will ultimately be limited by the available bandwidth of the external bias and signal circuitry, and this may have some influence on the performance of the APD for multi-photon responses as well.

REFERENCES

[1] Program ABINIT, http://www.abinit.org/.
[2] Program Wien2k, http://susi.theochem.tuwien.ac.at/
[3] O. Rubel, A. Bokhanchuk, S. J. Ahmed, and E. Assmann, Phys. Rev. B 90, 115202 (2014).
[4] F. Tran and P. Blaha, Phys. Rev. Lett. 102, 226401 (2009).
[5] B.K. Ridley, *Quantum processes in semiconductors*, Oxford University Press Inc., New York (1999).
[6] S. Derelle, S. Bernhardt, R. Haidar, J. Primot, J. Deschamps, and J. Rothman, *IEEE Trans. Electron. Dev. 56 (4), 569* (2009).
[7] R.A. Smith, *Semiconductors*, New York: Cambridge University Press (1978).
[8] G. Vignale, *Physics* 4, 48 (2011).
[9] L. Yang, J.D. Koralek, J. Orenstein, D.R. Tibbetts, J. L. Reno, and M.P. Lilly, *Phys. Rev. Lett.* 106 (2011).
[10] W. Riegler*, Nuclear Instruments and Methods in Physics Research* A 535, 287 (2004).
[11] E. Gatti and A. Geraci, *Nuclear Instruments and Methods in Physics Research A* 525, 623 (2004).
[12] M. Moresco, F. Bertazzi, and E. Bellotti, *IEEE J. Quant. El.* QE-47 4, 447 (2011).
[13] C. Bulutay, *Semicond. Sci. Technol.* 17, L59 (2002).
[14] E. Bellotti and F. Bertazzi, *Proc. of SPIE*, 8980, 89800R (2014).
[15] E.A. Kraut, *J. Vac. Sci. Technol. A* 7 (2), 420 (1989).
[16] S. A-B. Nasrallah, S. Mnasri, N. Sfina, N. Bouarissa, and M. Said, *J. Alloys and Compounds* **509**, 7677 (2011).
[17] M.V. Fischetti and S. Laux, *J. Appl. Phys. 80, 2234* (1996).
[18] K. Yeom, J.M. Hinckley, and J. Singh, *J. Appl. Phys. 80, 6773* (1996).

[19] E. Bellotti, F. Bertazzi, and M. Goano, *J. Appl. Phys. 101*, 123706 (2007).
[20] A.K. Storebø and T. Brudevoll, *J. Phys. Conf. Series* 647, 012051 (2015).
[21] G. Perrais, S. Derelle, L. Mollard, J-P. Chamonal, G. Destefanis, G. Vincent, S. Bernhardt, and J. Rothman, *J. Electron. Mater. 38*, 1790 (2009).
[22] F. Bertazzi, M. Moresco, M. Penna. M. Goano, and E. Bellotti, J. Electron. Mater. 39, 912 (2010).